JOURNAL OF COMPUTATIONAL PHYSICS 113, 62–74 (1994)

Three-Dimensional Fully Spectral Numerical Method for Mantle Convection with Depth-Dependent Properties

S. BALACHANDAR

Theoretical and Applied Mechanics Department, University of Illinois, Urbana, Illinois 61801

AND

D. A. YUEN

Minnesota Supercomputer Institute and Army High-Performance Computing and Research Center, University of Minnesota, Minneapolis, Minneapolis 55415

Received December 3, 1991; revised August 31, 1993

A semi-implicit fully spectral collocation method for the simulation of three-dimensional mantle convection with depth-dependent thermodynamic and transport properties is presented. The variable property Navier–Stokes equation expressed in terms of the primitive variable velocity and pressure is solved with the mass continuity and temperature equations. The periodic horizontal boundary conditions allow a Fourier expansion for the two horizontal directions. The stress-free, impermeable isothermal boundary conditions along with the depth dependent coefficients are handled with a Chebyshev expansion in the vertical direction. In the limit of an infinite Prandtl number appropriate to mantle convection, the inertial terms in the momentum equation are unimportant. In this case an explicit solution of a Poisson equation for pressure can be avoided; instead a fourth-order equation for vertical velocity can be solved. Simultaneous imposition of both impermeable and continuity boundary conditions during the vertical velocity evaluation is discussed. The pressure distributions on the top and bottom bounding planes were determined by means of an influence matrix technique. The numerical method employed here avoids time-splitting errors and enforces velocity boundary conditions and continuity over the entire domain, including the boundaries, to machine accuracy. Strongy time-dependent three-dimensional solutions up to a surface Rayleigh number of 1×10^7 have been obtained. Strong upwellings, pulsating chaotically, are formed by the collective merging of cylindrical plumes.

I. INTRODUCTION

The strongly time-dependent convective flow pattern in Earth's mantle is well evident through its manifestations in the various episodes of mountain-formation and continental break-up (Anderson [1], Richards *et al.* [2], and Campbell *et al.* [3]). A number of issues such as internal heating, phase transitions, and strongly depth-dependent thermodynamic and transport properties make this problem of thermal convection challenging. Earlier studies have made approximations at various levels to make this problem mathematically and computationally tractable. Rectangular geometry and axisymmetry have been invoked to render this inherently three-dimensional problem two-dimensional. Mantle convection is often studied in a cartesian framework rather than in a spherical shell to enhance spatial resolution. Simplifying assumptions have been employed in the models used to simulate mantle convection. The Boussinesq approximation, which neglects effects of compressibility and viscous heating, is often used to study mantle convection. Another important assumption often used is constant thermodynamic and transport properties.

From theoretical and laboratory investigations, there is mounting evidence to suggest that the thermal expansivity decreases strongly across the mantle [4], the thermal conductivity increases by a factor four across the mantle [5] and that viscosity increases by at least a factor of 10 across the mantle [6]. These strongly varying depth-dependencies can have a profound effect on the structure of large-scale mantle circulation and thermal plumes, as shown by recent two-dimensional simulations by Hansen *et al.* [7].

The compressibility effects can be accounted for with an anelastic approximation which lies between Boussinesq approximation and a fully compressible representation. The anelastic approximtion assumes that the resulting convective velocities are slow compared to the local sound speed.[1] Effectively, the sound speed is taken to be infinite and, consequently, sound waves are filtered out. The advantage of the anelastic approximation over the standard Boussinesq

[1] Since velocities in the mantle are on the order of a few centimeters per year, as opposed to the sound speed on the order of few kilometers per second, the anelastic approximation is certainly justified.

0021-9991/94 $6.00

approximation is that realistic depth-dependent variations of the thermodynamic and transport properties along with viscous heating can be taken into account. Moreover, the fluid now undergoes compression and expansion, although on a convective time-scale and not on the time-scale of sound waves. The advantage of the anelastic approximation over the full compressible formulation is that in the absence of sound waves, the time step restriction is less severe.

Our final objective is to focus attention on the effects of depth-dependent thermodynamic (mean density, mean temperautre, and expansivity) and transport (viscosity, conductivity) properties on turbulent thermal convection in infinite Prandtl number fluids, as applied to Earth's mantle. These effects have not been treated simultaneously up to now in the context of a three-dimensional model, although spherical axi-symmetric analyses including such effects have been performed (e.g., [8]). Specifically, we employ the anelastic model in our simulation to accurately account for these effects. It is our intention to simulate mantle convection at high Rayleigh numbers, well in the turbulent regime, and therefore the domain will be cast in a cartesian framework because of computational considerations. Periodic boundary conditions are assumed along the two horizontal directions to mimic an infinite layer. Stress-free, non-penetrative, isothermal boundary conditions, relevant to mantle convection are applied in the vertical direction. We will neglect the effects of temperature-dependence of viscosity and non-Newtonian rheology (nonlinear stress versus strain-rate constitutive relationship) to further simplify the problem. The effects of phase transitions in three-dimensional convection can also be simulated by using an effective thermal expansivity in both the momentum and energy equations [9].

The depth-dependent properties significantly complicate the continuity, momentum, and energy (temperature) equations. In particular, the depth-dependent properties introduce variable coefficients into the problem and implicit implementation of diffusion terms requires special care. In the limit of an infinite Prandtl number, the inertial terms in the momentum equations disappear and the velocity field simply follows the temperature field. Continuity can then be used to eliminate the horizontal velocities from the horizontal momentum equations to express pressure in terms of the vertical component of velocity. This, when substituted into the vertical momentum equation, provides a single higher order equation for the vertical component of velocity. This higher order equation requires boundary conditions in addition to the standard impermeability condition on the top and bottom bounding planes. These additional conditions are precisely the enforcement of continuity on the boundaries.

The purpose of this paper is to describe an efficient numerical algorithm to simulate compressible mantle convection with depth-dependent properties in the hard turbulent regime. In order to efficiently resolve the wide range of length scales associated with the turbulent spectrum we employ a spectral collocation method. A mixed Fourier–Chebyshev expansion for the flow variables provides superior spectral or exponential convergence and also accurately resolves the thermal and viscous boundary layers with minimal grid points. In the case of flows that include phase transitions the effective thermal expansivity peaks at the transition depths and high resolution is required to resolve the internal boundary layer developed in layered convection. Spectral methods with appropriate grid stretching along the homogeneous and inhomogeneous directions [10, 11] can efficiently resolve these internal structures. Due to their high accuracy, spectral methods are also very sensitive and require consistent and proper implementation of boundary conditions. Simultaneous enforcement of continuity and impermeability boundary conditions for the fourth-order vertical velocity equation is not straightforward. The fourth-order equation, when discretized leads to a linear algebraic system. Naive enforcement of the four boundary conditions would require sacrificing the enforcement of the governing equation not only at the boundary points but also at two other interior points. Here we describe a simple influence matrix technique to enforce both the continuity and impermeability conditions without affecting the enforcement of the governing equation in the interior. This approach is simpler than the conventional influence matrix method [12, 13] in which a Poisson equation is solved separately for pressure. Although we describe this methodology in the context of mantle convection, it can be extended to other problems as well to facilitate proper application of boundary conditions in the solution of higher order equations. In this paper, following Ku *et al.* [14] and Heidvogel [15], we also describe an efficient reduced matrix technique for the solution of Helmholtz-type linear equations with Neumann boundary conditions. In the context of spectral methods, the reduced matrix technique avoids the need for an influence matrix technique in order to enforce Neumann or mixed boundary conditions.

Section II describes the basic mathematical model and the relevant governing equations. The numerical method and the details of implementation are given in Section III. Section IV provides some sample results on a critical Rayleigh number. In order to demonstrate the numerical method's capabilities in the strongly time-dependent regime, results are also presented for the high Rayleigh number regime.

II. MATHEMATICAL FORMULATION

In the present anelastic model, the reference state for the thermodynamic variables, about which perturbations are

sought, is chosen to be time-independent, only a function of depth, and given by the adiabatic condition. The following expressions are the reference adiabatic depth-dependence of density (ϱ_a), temperature (T_a), and pressure (p_a),

$$\varrho_a(z) = \varrho_{a1}\left[1 + 2\frac{Di_1}{\gamma_1}(1-z)\right]^{1/2}$$
$$T_a = T_{a1}\exp\left[\frac{\gamma_1}{4}\left(1-\left(\frac{\varrho_{a1}}{\varrho_a}\right)^4\right)\right] \tag{1}$$
$$\frac{dp_a}{dz} = -\varrho_a g,$$

where subscript 1 corresponds to conditions at the top of the convective layer and z is the normalized depth, which ranges from 0 at the bottom to 1 at the top. The density profile is taken from the equation of state called the Adams–Williamson equation (e.g., [16]) applied with thermal expansivity a function of density [17]. This assumes that the background density lies along the adiabat. The adiabatic temperature profile is obtained by

$$\frac{dT_a}{dz} = \alpha(\varrho_a)\, Di\, T_a \tag{2}$$

In the above equations Di and γ are the dissipation number and Grüneisen parameter, respectively. The dissipation number is a measure of the scale height of the adiabat and the Grüneiser parameter is a measure of the an harmonic character of the equation of state (e.g., [18]). The density (ϱ'), temperature (θ'), and pressure (p') perturbations about their adiabatic state are defined as

$$\varrho' = \varrho - \varrho_a = \varrho_a(-\alpha\theta' + \chi p')$$
$$\theta' = T - T_a \tag{3}$$
$$p' = p - p_a,$$

where α is the coefficient of thermal expansion and χ is the isothermal compressibility. The above expressions for the thermodynamic variables can be substituted in the governing mass, momentum, and energy equations and normalized in the standard way [19]. The nondimensionalization process involves the scales

$$\text{length scale} = h, \qquad \text{velocity scale} = \kappa_1/h$$
$$\text{pressure scale} = \varrho_{a1}\kappa_1\nu_1/h^2, \qquad \text{temperature scale} = \Delta T,$$

where ΔT is the temperature difference across the convective layer of depth h, ν is the kinematic viscosity, κ is the thermal diffusivity. The thermodynamic and transport properties are assumed to vary with depth and are nondimensionalized with respect to their value at the top, to obtain the corresponding nondimensional quantities,

$$\bar{\varrho}_a = \frac{\varrho_a}{\varrho_{a1}}, \qquad \bar{\alpha} = \frac{\alpha}{\alpha_1}, \qquad \bar{\nu} = \frac{\nu}{\nu_1}, \qquad \bar{\kappa} = \frac{\kappa}{\kappa_1}, \qquad \bar{H} = \frac{H}{H_1} \tag{4}$$

where H is the internal heating. The specific heat at constant pressure, C_p, and the acceleration due to gravity, g, are assumed to be constant over the entire convective layer. The following nondimensional variables can then be introduced:

$$\mathrm{Ra} = \frac{\alpha_1 g\, \Delta T h^3}{\nu_1\kappa_1}, \qquad \mathrm{Pr} = \frac{\nu_1}{\kappa_1}, \qquad \mathrm{Di} = \frac{\alpha_1 g h}{C_p}$$
$$\varepsilon = \alpha_1 \Delta T, \qquad K = \frac{\chi_1\varrho_{a1}\kappa_1\nu_1}{h^2\alpha_1\Delta T}, \qquad A = \frac{H_1 h^2}{C_p \Delta T \kappa_1}. \tag{5}$$

For Earth's mantle the nondimensional parameter ε is only a few percent [20] and K lies between 10^{-5} and 10^{-6} [19]. Therefore, both these parameters play an unimportant role and, hence, we can set $\varepsilon = K = 0$. This *anelastic liquid* approximation leads to the following governing equations for the nondimensional velocity, temperature, and pressure perturbations, (u_i, θ, p),

$$\nabla\cdot(\bar{\varrho}_a\mathbf{u}) = 0$$
$$0 = -\frac{\partial p}{\partial x_i} + \frac{\partial \tau_{ki}}{\partial x_k} + \delta_{i3}\, Ra\, \bar{\varrho}_a\bar{\alpha}\theta$$
$$\bar{\varrho}_a\frac{D\theta}{Dt} + \mathrm{Di}\,\bar{\alpha}\bar{\varrho}_a w\theta = \frac{\mathrm{Di}}{\mathrm{Ra}}\tau_{ik}\frac{\partial u_i}{\partial x_k} + \frac{\partial}{\partial x_i}\left(\bar{k}\frac{\partial\theta}{\partial x_i}\right) + \frac{\partial}{\partial z}\left(\bar{k}\frac{\partial \overline{T_a}}{\partial z}\right) + A\bar{\varrho}_a\bar{H} \tag{6}$$
$$\tau_{ik} = \bar{\eta}\left(\frac{\partial u_i}{\partial x_k} + \frac{\partial u_k}{\partial x_i} - \frac{2}{3}\delta_{ik}\nabla\cdot\mathbf{u}\right)$$
$$\text{with} \quad \bar{\eta} = \bar{\nu}\bar{\varrho}_a,$$

where $\bar{k} = k/k_1$ is the nondimensional thermal conductivity at the top of the convective layer and thermal conductivity and diffusivity are related as $k_1 = \kappa_1\varrho_{a1}C_p$. Comparison between an anelastic liquid approximation and the entropy approach for the energy equation was made by Glatzmaier [21]. Differences of a few percent were observed. In the above equations, the infinite Prandtl number limit appropriate to mantle convection is assumed to eliminate the inertia terms in the momentum equation. For simplicitly the bulk viscosity has been neglected in the expression for the stress tensor. The momentum equations are not prognostic and therefore the velocity field is determined by the temperature field. Continuity and boundary conditions place constraints on this driven velocity field.

III. NUMERICAL METHOD

Numerical methods for the simulation of three-dimensional, constant property, finite or infinite Prandtl number, thermal convection at moderate to large Rayleigh numbers are common [22, 23, 24, 25]. These simulations employ a variety of numerical methods ranging from spectral to finite difference methods. We extend the methodology from its present canonical form to include the effects of depth-dependent properties such as depth-dependent thermal expansivity, background density from compressibility, internal heat generation, and thermal conductivity. These important aspects relevant to mantle convection introduce additional terms into the governing equations and result in coefficients which depend on the vertical coordinate.

The numerical procedure to be employed in advancing the flow field can be outlined in the following four steps:

(1) Temperature evolution is governed by the energy equation which can be written as

$$\frac{\partial \theta}{\partial t} = N(\mathbf{u}, \theta) + L(\theta),$$

where

$$N(\mathbf{u}, \theta) = -\mathbf{u}\cdot\nabla\theta - Di\bar{\alpha}w\theta + \frac{Di}{Ra}\frac{1}{\overline{\varrho_a}}\tau_{ik}\frac{\partial u_i}{\partial x_k} + A\bar{H} + \frac{1}{\overline{\varrho_a}}\frac{\partial}{\partial z}\left(\bar{k}\frac{\partial \overline{T_a}}{\partial z}\right) \tag{7}$$

and

$$L(\theta) = \frac{1}{\overline{\varrho_a}}\frac{\partial}{\partial x_i}\left(\bar{k}\frac{\partial \theta}{\partial x_i}\right).$$

In the above equation, $N(\mathbf{u}, \theta)$ includes the nonlinear (advection, buoyancy, and viscous heating) and time-independent (internal heating and mean adiabatic diffusion) terms and $L(\theta)$ represents the linear diffusion term in the energy equation. The energy equation being the only (prognostic) equation with a time derivative, as a first step, the temperature field is advanced in time with a three-stage Runge–Kutta scheme for the nonlinear terms and an implicit Crank–Nicholson scheme for the linear diffusion term.

(2) The vertical momentum equation can be written as

$$\nabla^2 w + \left(F(z) + \frac{d\ln\bar{\eta}}{dz}\right)\frac{\partial w}{\partial z} + H(z)w = \frac{1}{\bar{\eta}}\frac{\partial p}{\partial z} - \frac{\mathrm{Ra}\,\overline{\varrho_a}\bar{\alpha}}{\bar{\eta}}\theta$$

where

$$F(z) = \frac{d\ln\bar{\eta}}{dz} - \frac{1}{3}\frac{d\ln\overline{\varrho_a}}{dz},$$

$$H(z) = \frac{2}{3}\frac{d\ln\bar{\eta}}{dz}\frac{d\ln\overline{\varrho_a}}{dz} - \frac{1}{3}\frac{d^2\ln\overline{\varrho_a}}{dz^2}. \tag{8}$$

Note that this equation for the vertical velocity is linear with variables coefficients which are functions of only the vertical coordinate. The above equation must be solved with impermeability boundary condition ($w(z=0, 1)=0$) on the top and bottom boundaries. A straightforward solution is not possible since the pressure gradient on the right-hand side couples w with the other components of velocity.

A common approach to solving this problem is to obtain a Poisson equation for pressure from the divergence of the momentum equation. The pressure Poisson equation is solved to obtain pressure which can then be used in Eq. (8). But, in the solution of the pressure Poisson equation no natural pressure boundary condition is available, and continuity is often enforced at the boundary [12, 13, 26, 14, 27]. The pressure poisson and the momentum equations are then coupled through this continuity boundary condition. The influence matrix method can be used to resolve this coupling [12, 13].

In the present context, with the absence of the nonlinear terms in the momentum equations, a simplified approach which avoids explicit solution of the pressure Poisson equation is possible. By eliminating the horizontal components of velocity between the continuity and the two horizontal momentum equations, pressure can be directly related to the vertical component of velocity. This relation becomes algebraic when expressed in Fourier space as

$$\hat{p} = \bar{\eta}F\hat{w} - \bar{\eta}\hat{G} + \frac{\bar{\eta}}{k_x^2 + k_y^2}\left[\frac{d^2\hat{G}}{dz^2} + \frac{d\ln\bar{\eta}}{dz}\frac{d\hat{G}}{dz}\right],$$

where

$$\hat{G} = \frac{d\hat{w}}{dz} + \frac{d\ln\overline{\varrho_a}}{dz}\hat{w}. \tag{9}$$

Here the hats represent Fourier coefficients obtained from Fourier transformations along the two horizontal directions. The above equation can be substituted into the Fourier transform of Eq. (8) to obtain a single fourth-order equation for the vertical component of velocity. The appropriate boundary conditions for this higher order equation are the impermeability condition and the continuity equation. Here, the enforcement of continuity on the boundary can be transformed into a vertical velocity boundary condition by taking the vertical derivative of the continuity equation

$$\frac{d^2 w}{dz^2} + \frac{d}{dz}\left(\frac{1}{\overline{\varrho_a}}\frac{d\overline{\varrho_a}}{dz}w\right) = 0 \qquad \text{at} \quad z = 0, 1. \tag{10}$$

The higher order equation and boundary conditions for the vertical component of velocity are now completely decoupled and can be computed from the temperature field.

(3) As the third step, the pressure perturbation is obtained from the vertical velocity through Eq. (9).

(4) From Eq. (6) the x- and y-momentum equation can be written as

$$\nabla^2 u + \frac{d\ln\bar{\eta}}{dz}\frac{\partial u}{\partial z} = \frac{1}{\eta}\frac{\partial p}{\partial x} - \frac{1}{\bar{\eta}}F\frac{\partial w}{\partial x}$$
$$\nabla^2 v + \frac{d\ln\bar{\eta}}{dz}\frac{\partial v}{\partial z} = \frac{1}{\eta}\frac{\partial p}{\partial y} - \frac{1}{\bar{\eta}}F\frac{\partial w}{\partial y}. \tag{11}$$

From the computed pressure and vertical velocity fields, the above equations are solved to obtain u and v at the new time level.

We employ a fully spectral Fourier–Chebyshev collocation methodology to implement the above outlined numerical scheme. The spectral method is chosen for its exponential or spectral convergence and superior resolution of a wide range of length scales associated with turbulent flows. Unlike lower order accurate finite difference and finite element methods, spectral methods are unforgiving. Physically meaningful boundary conditions and accurate implementation of these boundary conditions are essential in obtaining a scheme that is successful overall. These implementation issues in the context of a spectral simulation will be discussed below.

The variable coefficients and the resulting inhomogeneity along the vertical direction will be accommodated with a Chebyshev expansion for the flow field in the vertical direction. The periodic horizontal boundary conditions are implemented with a Fourier expansion in these directions. The Fourier–Chebyshev expansion provides the following natural equi-spaced grid points in the horizontal directions and Chebyshev Gauss–Lobatto points in the vertical direction,

$$x_i = \frac{L_x(i-1)}{N_x}, \qquad y_j = \frac{L_y(j-1)}{N_y},$$
$$z_l = \frac{1}{2}\left(1 - \cos\left[\frac{\pi(l-1)}{N_z - 1}\right]\right), \tag{12}$$

where N_x, N_y, and N_z are the number of points along the three cartesian directions and L_x and L_y are the aspect ratios along the horizontal directions. The following forward and backward discrete Fourier transforms in the horizontal directions can be defined

$$\begin{Bmatrix}\hat{u}\\ \hat{v}\\ \hat{w}\\ \hat{\theta}\end{Bmatrix}(k_x, k_y, z_l) = \sum_{i=1}^{N_x}\sum_{j=1}^{N_y}\begin{Bmatrix}u\\ v\\ w\\ \theta\end{Bmatrix}(x_i, y_j, z_l) \times \exp\left(\imath\frac{2\pi}{L_x}k_x x_i\right)\exp\left(\imath\frac{2\pi}{L_y}k_y y_j\right), \tag{13}$$

where

$$k_x = -\left(\frac{N_x}{2} - 1\right), \ldots, 0, \ldots, \frac{N_x}{2}$$
$$k_y = -\left(\frac{N_y}{2} - 1\right), \ldots, 0, \ldots, \frac{N_y}{2}$$
$$\begin{Bmatrix}u\\ v\\ w\\ \theta\end{Bmatrix}(x_i, y_j, z_l) = \frac{1}{N_x N_y}\sum_{k_x}\sum_{k_y}\begin{Bmatrix}\hat{u}\\ \hat{v}\\ \hat{w}\\ \hat{\theta}\end{Bmatrix}(k_x, k_y, z_l) \times \exp\left(-\imath\frac{2\pi}{L_x}k_x x_i\right)\exp\left(-\imath\frac{2\pi}{L_y}k_y y_j\right). \tag{14}$$

In the above equations $\hat{u}$, $\hat{v}$, $\hat{w}$, and $\hat{\theta}$ represent the Fourier coefficients of velocity u, v, w, and perturbation temperature θ, and k_x and k_y are the wave-numbers. These transforms can be efficiently implemented with fast Fourier transforms available as highly optimized library routines in CRAY computers.

(1) *Temperature Step*

Time-marching of the temperature equation (Eq. (7)) uses an explicit three-stage Runge–Kutta scheme for the nonlinear terms and an implicit Crank–Nicholson scheme for the linear terms. The discretized temperature equation can then be written as

$$\mathbf{u}^0 = \mathbf{u}(t^n), \qquad \theta^0 = \theta(t^n)$$
$$\left\{\begin{array}{c} J^0 = \Delta t\, N_D(\mathbf{u}^0, \theta^0) \\ \theta^1 = \theta^0 + \frac{1}{3}J^0 + c_0[L_D(\theta^0) + L_D(\theta^1)] \\ c_0 = \frac{1}{6}\end{array}\right\} \text{Stage I}$$
$$\left\{\begin{array}{c} J^1 = \Delta t\, N_D(\mathbf{u}^1, \theta^1) - \frac{5}{9}J^0 \\ \theta^2 = \theta^1 + \frac{15}{16}J^1 + c_1[L_D(\theta^1) + L_D(\theta^2)] \\ c_1 = \frac{5}{24}\end{array}\right\} \text{Stage II} \tag{15}$$
$$\left\{\begin{array}{c} J^2 = \Delta t\, N_D(\mathbf{u}^2, \theta^2) - \frac{153}{128}J^1 \\ \theta^3 = \theta^2 + \frac{8}{15}J^2 + c_2[L_D(\theta^2) + L_D(\theta^3)] \\ c_2 = \frac{1}{8}\end{array}\right\} \text{Stage III}$$
$$\mathbf{u}(t^{n+1}) = \mathbf{u}^3, \qquad \theta(t^{n+1}) = \theta^3,$$

where N_D and L_D are the discrete versions of the nonlinear and linear operators defined in Eq. (7). At each ($m = 0$, 1, and 2) stage of the Runge–Kutta scheme the nonlinear terms, J^m, and the explicit part of the linear terms, $\theta^m + c_m L(\theta^m)$, are first computed to form the right-hand side of the equation, R_θ. This operation is performed in real space, since the nonlinear terms are represented by a simple product in real space as opposed to a convolution in

spectral space. The resulting Helmholtz equation for the unknown temperature can then be Fourier-transformed along the two periodic directions to obtain the following set of decoupled ODEs for the Fourier coefficients of the temperature field (for each horizontal wave-number combination k_x, k_y):

$$\frac{1}{\bar{k}}\left[\frac{d}{dz}\left(\bar{k}\frac{d\hat{\theta}^{m+1}}{dx}\right)\right]-\left[\left(\frac{2\pi k_x}{L_x}\right)^2+\left(\frac{2\pi k_y}{L_y}\right)^2+\frac{\overline{\varrho_a}}{c_m\bar{k}}\right]\times\hat{\theta}^{m+1}=\hat{R}_\theta. \tag{16}$$

With a Chebyshev discretization in the z direction the above equation reduces to the matrix problem

$$\mathbf{T}_m\hat{\theta}^{m+1}-\lambda_T\mathbf{I}\hat{\theta}^{m+1}=\hat{R}_\theta, \tag{17}$$

where $\mathbf{T}_m$ is a square matrix of size $(N_z+1)\times(N_z+1)$ obtained from the Chebyshev first derivative matrix $\mathbf{D}_{c1}$ [28], $\mathbf{I}$ is an identity matrix of the same size, and λ_T is a constant which depends on k_x and k_y. From Eq. (16) the matrix $\mathbf{T}_m$ and the constant λ_T can be defined as

$$(\mathbf{T}_m)_{ij}=\frac{\bar{k}(z_p)}{\bar{k}(z_i)}(\mathbf{D}_{c1})_{ip}(\mathbf{D}_{c1})_{pj}+\frac{\overline{\varrho_a}(z_i)}{c_m\bar{k}(z_i)}\delta_{ij},$$
$$\lambda_T=\left(\frac{2\pi k_x}{L_x}\right)^2+\left(\frac{2\pi k_y}{L_y}\right)^2. \tag{18}$$

In the above equation as well as all the other equations to follow, no summation over the index i but summation over all other repeated indices is assumed.

In the above matrix formulation the isothermal boundary condition can be incorporated by modifying the first and last rows of $\mathbf{T}_m$ by [1 0 0...0] and [0 0 0...1], respectively, and also appropriately replacing the first and last elements of the right-hand side [28]. Equation (17) for the temperature coefficients can then be efficiently solved by the matrix diagonalization technique. This matrix diagonalization technique involves the computation of eigenvalues and eigenvectors of the modified matrix operator. Since these three matrices, for $m=0$, 1, 2, are independent of both time and horizontal wave numbers, the eigenvalues and eigenvectors can be computed once and for all and stored for repeated later use. The computation of $\hat{\theta}^{m+1}$ for each horizontal wave-number combination (k_x, k_y) then reduces to two matrix–vector multiplications [28] which can be performed in a highly efficient manner in vector machines like the CRAY.

(2) *Vertical Velocity Step*

The Fourier transform of the vertical momentum equation (Eq. (8)) can be discretized and written as

$$(\mathbf{M}_1)_{ij}\hat{w}(z_j)=\frac{1}{\bar{\eta}}(z_i)\left((\mathbf{D}_{c1})_{ij}\hat{p}(z_j)-\mathrm{Ra}\,\overline{\varrho_a}(z_i)\,\bar{\alpha}(z_i)\,\hat{\theta}(z_i)\right), \tag{19}$$

where $\mathbf{M}_1$ is a square matrix of size $N_z\times N_z$ given by

$$(\mathbf{M}_1)_{ij}=(\mathbf{D}_{c2})_{ij}+\left(F+\frac{d\ln\bar{\eta}}{dz}\right)(z_i)\,(\mathbf{D}_{c1})_{ij}-(k_x^2+k_y^2-H(z_i))\,\delta_{ij}$$

and $\mathbf{D}_{c1}$ and $\mathbf{D}_{c2}$ are the Chebyshev first and second derivative matrices [29]. Similarly, the discrete version of the pressure equation (Eq. (9)) can now be written as

$$\hat{p}=\mathbf{M}_2\hat{w}=\left[\mathbf{M}_3+\frac{\mathbf{M}_4}{k_x^2+k_y^2}\right]\hat{w},$$

where

$$(\mathbf{M}_3)_{ij}=-\bar{\eta}(z_i)(\mathbf{D}_{c1})_{ij}+\bar{\eta}\left(F-\frac{d\ln\overline{\varrho_a}}{dz}\right)(z_i)\,\delta_{ij} \tag{20}$$

and

$$(\mathbf{M}_4)_{ij}=\bar{\eta}(z_i)\left[(\mathbf{D}_{c2})_{ip}+\frac{d\ln\bar{\eta}}{dz}(z_i)(\mathbf{D}_{c1})_{ip}\right]\times\left[(\mathbf{D}_{c1})_{pj}+\frac{d\ln\overline{\varrho_a}}{dz}(z_p)\,\delta_{pj}\right],$$

where the matrix operators $\mathbf{M}_2$, $\mathbf{M}_3$, and $\mathbf{M}_4$ are of size $N_z\times N_z$. By substituting Eq. (20) in Eq. (19) a linear system corresponding to a single fourth-order equation for the Fourier coefficients of the vertical velocity can be obtained as

$$\mathbf{M}_5\hat{w}=-\frac{1}{\bar{\eta}}\,\mathrm{Ra}\,\overline{\varrho_a}\bar{\alpha}\hat{\theta}, \tag{21}$$

where

$$(\mathbf{M}_5)_{ij}=(\mathbf{M}_1)_{ij}-\frac{1}{\bar{\eta}}(z_i)(\mathbf{D}_{c1})_{ip}(\mathbf{M}_2)_{pj}.$$

The above algebraic system should be solved with both impermeable and continuity boundary conditions. The impermeable condition can be easily enforced by defining a modified matrix operator $\mathbf{M}_5^*$, which is equivalent to $\mathbf{M}_5$ but with the top and bottom rows appropriately replaced, and zeroing the first and last elements of the right-hand side. In essence, at the boundary points the no penetration boundary condition is enforced instead of the governing equation. Naive enforcement of the additional continuity boundary condition (Eq. (10)) corresponding to the higher order system would require sacrificing the enforcement of the governing equation at a two interior nodes as well. A solution at this stage without enforcing continuity bound-

ary conditions is not feasible since the matrix operator $\mathbf{M}_5^*$ is singular and non-invertable. Suppose, ξ and β are the appropriate pressure boundary conditions ($\hat{p}(z=0)=\xi$, $\hat{p}(z=1)=\beta$) which will satisfy boundary continuity; these boundary pressures need to be included in the definition of $\mathbf{M}_5^*$. By noting that the matrix operator $\mathbf{M}_2$ provides pressure when operated on $\hat{w}$, the pressure boundary conditions can be enforced by modifying the Chebyshev first derivative matrix (which operates on $\mathbf{M}_2$) as

$$\begin{bmatrix} (\mathbf{D}_{c1})_{11} & (\mathbf{D}_{c1})_{12} & \cdots & (\mathbf{D}_{c1})_{1N_z} \\ (\mathbf{D}_{c1})_{21} & (\mathbf{D}_{c1})_{22} & \cdots & (\mathbf{D}_{c1})_{2N_z} \\ \vdots & \vdots & \vdots & \vdots \\ (\mathbf{D}_{c1})_{N_z1} & (\mathbf{D}_{c1})_{N_z2} & \cdots & (\mathbf{D}_{c1})_{N_zN_z} \end{bmatrix} \begin{bmatrix} \xi \\ \hat{p}(z_2) \\ \vdots \\ \beta \end{bmatrix}$$
$$= \begin{bmatrix} 0 & (\mathbf{D}_{c1})_{12} & \cdots & 0 \\ 0 & (\mathbf{D}_{c1})_{22} & \cdots & 0 \\ \vdots & \vdots & \vdots & \vdots \\ 0 & (\mathbf{D}_{c1})_{N_z2} & \cdots & 0 \end{bmatrix} \begin{bmatrix} \hat{p}(z_1) \\ \hat{p}(z_2) \\ \vdots \\ \hat{p}(z_{N_z}) \end{bmatrix}$$
$$+ \begin{bmatrix} \xi(\mathbf{D}_{c1})_{11} + \beta(\mathbf{D}_{c1})_{1N_z} \\ \xi(\mathbf{D}_{c1})_{21} + \beta(\mathbf{D}_{c1})_{2N_z} \\ \vdots \\ \xi(\mathbf{D}_{c1})_{N_z1} + \beta(\mathbf{D}_{c1})_{N_zN_z} \end{bmatrix}. \tag{22}$$

The matrix on the right-hand side, $(\mathbf{D}_{c1}^*)$, is the Chebyshev first derivative matrix with the first and last columns replaced by zeros. Therefore in the definition of $\mathbf{M}_5^*$ the Chebyshev first derivative matrix can be replaced by $\mathbf{D}_{c1}^*$ and the influence of the pressure boundary conditions can be moved to the right-hand side and Eq. (21) can be rewritten as

$$(\mathbf{M}_5^{**})_{ij}\,\hat{w}(z_j) = -\frac{1}{\bar{\eta}}\,(\mathrm{Ra}\,\overline{\varrho_a}\bar{\alpha}\hat{\theta}(z_i) - \xi(\mathbf{D}_{c1})_{i1} - \beta(\mathbf{D}_{c1})_{iN_z}), \tag{23}$$

where $\mathbf{M}_5^{**}$ is the same as $\mathbf{M}_5$ with both impermeable and pressure boundary conditions enforced. The vertical velocity can now be evaluated by inverting $\mathbf{M}_5^{**}$, which is non-singular and invertable. $\mathbf{M}_5^{**}$ is independent of time, therefore it can be computed, inverted, and stored for later use at the very beginning. Since this matrix operator is dependent upon k_x and k_y, storage of $\mathbf{M}_5^{**}$ for all wave numbers is proportional to $N_x\,N_y\,N_z^2$. Retaining all these matrices in core memory is prohibitive for all but small grids. For larger problems these matrices can be computed in a preprocessing step and stored on a fast access disk in CRAY systems. At any time during the simulation, only two of these matrices are retained in core memory, while computations are performed on the first; the second can be read into memory in an asynchronous manner from the fast access storage. Such asynchronous I/O neither increases the CPU time nor the wall clock turnaround time in any significant manner. Further reduction in storage and memory is possible by utilizing symmetries built into the problem. For example, in the case of a square plan-form there is an eightfold symmetry in the horizontal plane.

The boundary pressures ξ and β are unknowns and need to be evaluated through the influence matrix technique. The continuity on the boundary (Eq. (10)) is used to evaluate ξ and β. Substituting Eq. (23) into the Fourier transform of Eq. (10) we obtain

$$(\mathbf{M}_6)_{ij}\,[-\mathrm{Ra}\,\overline{\varrho_a}\bar{\alpha}\hat{\theta}(z_j) + \xi(\mathbf{D}_{c1})_{j1} + \beta(\mathbf{D}_{c1})_{jN_z}] = 0,$$

where

$$(\mathbf{M}_6)_{ij} = \left[(\mathbf{D}_{c2})_{ip} + (\mathbf{D}_{c1})_{iq}\,\frac{d\ln\overline{\varrho_a}}{dz}\,(z_q)\,\delta_{qp}\right](\mathbf{M}_5^{**})_{pj}^{-1}\,\frac{1}{\bar{\eta}(z_j)} \tag{24}$$

for $i=1$ and N_z, corresponding to the bottom and top boundaries. The above two boundary conditions can be rewritten in the form

$$\begin{bmatrix} (\mathbf{M}_6)_{1j}(\mathbf{D}_{c1})_{j1} & (\mathbf{M}_6)_{1j}(\mathbf{D}_{c1})_{jN_z} \\ (\mathbf{M}_6)_{N_zj}(\mathbf{D}_{c1})_{j1} & (\mathbf{M}_6)_{N_zj}(\mathbf{D}_{c1})_{jN_z} \end{bmatrix} \begin{bmatrix} \xi \\ \beta \end{bmatrix}$$
$$= \begin{bmatrix} (\mathbf{M}_6)_{1j}\,\mathrm{Ra}\,\overline{\varrho_a}\bar{\alpha}\hat{\theta}(z_j) \\ (\mathbf{M}_6)_{N_zj}\,\mathrm{Ra}\,\overline{\varrho_a}\bar{\alpha}\hat{\theta}(z_j) \end{bmatrix}, \tag{25}$$

where the matrix on the left-hand side is the influence matrix. The elements of this influence matrix correspond to boundary divergences due to unit pressure perturbations at the boundaries. The right-hand side represents the boundary divergences corresponding to the particular solution, with arbitrary zero pressure boundary condition. The solution vector $[\xi\beta]^T$ corresponds to the correct boundary pressure which will nullify the divergence due to the particular solution. The influence matrix is frozen in time and is only (2×2) in size; therefore it can be computed once and for all and stored at the beginning for each horizontal wavenumber combination. Each time step the computational methodology involved in the vertical-velocity evaluation can be summarized by the following three steps:

(1) Calculate the right-hand side of Eq. (25)

(2) Solve Eq. (25) for ξ and β

(3) Solve for $\hat{w}$ in Eq. (23).

The above steps are repeated for each k_x and k_y, except at $k_x=k_y=0$. This mean vertical velocity can be shown to be identically equal to zero.

(3) *Pressure Step.*

Once the vertical velocity is known, the pressure can be computed from the algebraic relation in Eq. (20). Here, the

matrix operators, $\mathbf{M}_3$ and $\mathbf{M}_4$, depend only on the grid definition in the vertical direction and on the variation of adiabatic density and viscosity with depth. Therefore $\mathbf{M}_3$ and $\mathbf{M}_4$ can be computed once at the very beginning, and, at each time step, $\mathbf{M}_2$ can be constructed without much computational effort. This operation is repeated for each horizontal wave-number combination, except at $k_x = k_y = 0$. The mean pressure variation with depth is evaluated from

$$\frac{d\bar{p}|_{00}}{dz} = \mathrm{Ra}\,\overline{\varrho_a \alpha \theta}|_{00} \tag{26}$$

which can be solved by inverting the Chebyshev first-derivative matrix. Before inverting the matrix, a Dirichlet boundary condition, $\hat{p}|_{00}(z=1)=0$, is applied to anchor the mean pressure at the top.

(4) *Horizontal Velocity*

The *x-momentum equation* (Eq. (11)) can be Fourier-transformed along the horizontal directions and discretized in the vertical direction to obtain the algebraic system,

$$(\mathbf{V}_1)_{ij}\,\hat{u}(z_j) - (k_x^2 + k_y^2)\,\mathbf{I}_{ij}\hat{u}(z_j) = \frac{\imath k_x}{\bar{\eta}}(\hat{p} - F\hat{w})(z_i)$$
$$(\mathbf{V}_1)_{ij} = (\mathbf{D}_{c2})_{ij} + \frac{d\ln\bar{\eta}}{dz}(z_i)(\mathbf{D}_{c1})_{ij}, \tag{27}$$

where $\mathbf{V}_1$ is a square matrix operator of size $N_z \times N_z$. The boundary conditions appropriate to mantle convection are the stress-free boundary conditions, $(\partial u/\partial z)(z=0, 1)=0$. These pure Neumann boundary conditions can be built into the operator using the reduced matrix technique [14, 15]). In this technique a reduced matrix, $\tilde{\mathbf{V}}_1$, of size $(N_z-2)\times(N_z-2)$ which incorporates the Neumann boundary conditions, will be derived from $\mathbf{V}_1$. The reduced operator $\tilde{\mathbf{V}}_1$ when operating *only* on the interior data points will have the same effect as the full operator $\mathbf{V}_1$ operating on all the points, including the boundary points. $\tilde{\mathbf{V}}_1$ can be derived by writing the full operator as

$$\sum_{j=1}^{N_z}(\mathbf{V}_1)_{ij}\,\hat{u}(z_j) = \sum_{j=2}^{N_z-1}(\mathbf{V}_1)_{ij}\,\hat{u}(z_j) + (\mathbf{V}_1)_{i1}\,\hat{u}(z_1) + (\mathbf{V}_1)_{iN_z}\,\hat{u}(z_{N_z}), \tag{28}$$

where the boundary values of $\hat{u}$ are isolated. Since the reduced operator operates only on the interior points, the idea is to express the boundary values of $\hat{u}$ in terms of the interior points. For this purpose the Neumann boundary conditions can be written as

$$\begin{aligned}\sum_{i=1}^{N_z}(\mathbf{D}_{c1})_{1i}\,\hat{u}(z_i) &= \sum_{i=2}^{N_z-1}(\mathbf{D}_{c1})_{1i}\,\hat{u}(z_i) + (\mathbf{D}_{c1})_{11}\,\hat{u}(z_1) + (\mathbf{D}_{c1})_{1N_z}\,\hat{u}(z_{N_z}) = 0\\ \sum_{i=1}^{N_z}(\mathbf{D}_{c1})_{N_z i}\,\hat{u}(z_i) &= \sum_{i=2}^{N_z-1}(\mathbf{D}_{c1})_{N_z i}\,\hat{u}(z_i) + (\mathbf{D}_{c1})_{N_z 1}\,\hat{u}(z_1) + (\mathbf{D}_{c1})_{N_z N_z}\,\hat{u}(z_{N_z}) = 0.\end{aligned} \tag{29}$$

The above two equations can be solved to express $\hat{u}(z_1)$ and $\hat{u}(z_{N_z})$ in terms of the interior values. These, when substituted in Eq. (28), result in

$$\sum_{j=2}^{N_z-1}\left[(\mathbf{V}_1)_{ij} + \frac{(\mathbf{V}_1)_{i1}(\mathbf{D}_{c1})_{N_zN_z}(\mathbf{D}_{c1})_{1j} + (\mathbf{V}_1)_{iN_z}(\mathbf{D}_{c1})_{11}(\mathbf{D}_{c1})_{1j}}{(\mathbf{D}_{c1})_{N_z1}(\mathbf{D}_{c1})_{1N_z} - (\mathbf{D}_{c1})_{11}(\mathbf{D}_{c1})_{N_zN_z}} - \frac{(\mathbf{V}_1)_{i1}(\mathbf{D}_{c1})_{1N_z}(\mathbf{D}_{c1})_{N_zj} - (\mathbf{V}_1)_{iN_z}(\mathbf{D}_{c1})_{N_z1}(\mathbf{D}_{c1})_{1j}}{(\mathbf{D}_{c1})_{N_z1}(\mathbf{D}_{c1})_{1N_z} - (\mathbf{D}_{c1})_{11}(\mathbf{D}_{c1})_{N_zN_z}}\right]\times\hat{u}(z_j), \tag{30}$$

where the terms within the square bracket represent the (i,j)th element of the reduced operator $\tilde{\mathbf{V}}_1$. In terms of the reduced matrix, Eq. (27) can be rewritten as

$$(\tilde{\mathbf{V}}_1)_{ij}\,\hat{u}(z_j) - (k_x^2 + k_y^2)\,\mathbf{I}_{ij}\,\hat{u}(z_j) = \frac{\imath k_x}{\bar{\eta}}(\hat{p} - F\hat{w})(z_i), \tag{31}$$

where i and j range from 2 to $N_z - 1$. The above linear algebraic system can be efficiently solved with the matrix diagonalization technique [28] by obtaining the eigenvalues and eigenvectors of $\tilde{\mathbf{V}}_1$. Since this operator neither depends on time nor on the wave numbers, its eigenvalues and eigenvectors can be precomputed and stored in memory. Once the interior $\hat{u}$'s are obtained from Eq. (31), its boundary values can be evaluated by solving Eq. (29). It should be pointed out that using the reduced matrix technique other Dirichlet, Robin, and mixed boundary conditions can be handled as well with relative ease. Homogeneous boundary conditions, as in the present case, leave the right-hand side of the reduced equation (Eq. (31)) unaltered. Inhomogeneous boundary conditions will introduce additional terms to the right-hand side.

The *y*-momentum equation is very similar to the *x*-momentum equation and the corresponding solution procedure is identical. The resulting reduced matrix for the evaluation of $\hat{v}$ is again $\tilde{\mathbf{V}}_1$. In the case of $k_x = 0$ modes in the evaluation of $\hat{u}$ and, similarly, $k_y = 0$ modes in the evaluation of $\hat{v}$ the forcing term (the right-hand side of Eq. (31)) vanishes. This results in trivial zero solutions which need not be computed explicitly. The above four steps complete the time-marching procedure.

IV. RESULTS

The numerical simulation is first tested in the limit of depth-independent constant thermodynamic and transport properties. In this limit the present simulation was a bench mark against earlier three-dimensional simulations of Travis *et al.* [25]. The impermeable, free-slip, thermally insulating side walls employed in their finite difference computations were approximately enforced in the present spectral simulation with periodic boundary conditions. This approximation was improved by restricting the initial temperature and velocity perturbation to be a pure sine or cosine series along the horizontal directions. Several of the test convection cases reported by Travis *et al.* [25] were successfully repeated with the present code. The present numerical simulation was further validated with the calculation of the critical Rayleigh number as a function of the aspect ratio, the ratio of width to depth of the physical domain, in the limit of constant properties. The result is presented as the solid line in Fig. 1. The observed critical Rayleigh number of $27\pi^4/4$ and the critical aspect ratio of $2\sqrt{2}$ agree with existing linear stability results [30].

First we shall consider the effects of depth-dependent properties on critical Rayleigh numbers. For this purpose, we employ the following plausible depth dependence for adiabatic density ($\bar{\varrho}_a$), Grünaisen parameter ($\bar{\gamma}$), adiabatic temperature ($\bar{T}_a$), thermal expansivity ($\bar{\alpha}$), and thermal conductivity ($\bar{k}$) [17],

$$\bar{\varrho}_a(z)=\left[1+\frac{2Di}{\gamma_1}(1-z)\right]^{1/2},$$
$$\bar{\gamma}(z)=(\bar{\varrho}_a)^{-4}, \qquad \bar{\alpha}(z)=(\bar{\varrho}_a)^{-6} \tag{32}$$
$$\bar{T}_a(z)=\bar{T}_a(1)\exp\left(\frac{\gamma_1}{4}[1-(\bar{\varrho}_a)^{-4}]\right), \qquad \bar{k}(z)=(\bar{\varrho}_a)^4,$$

where γ_1 is Grüneisen parameter evaluated at the top. With $Di=0.4$ and $\gamma_1=1.4$, we obtain a adiabatic density contrast of 1.25 between the bottom and the top. The corresponding adiabatic temperature, Grünaisen parameter, thermal expansivity, and thermal conductivity contrasts are 1.23, 2.44, 0.26, and 2.47, respectively. Viscosity increase with depth is more dramatic and influences the resulting flow field significantly. The following two viscosity functions which increases with depth with varying bottom to top viscosity contrast, ζ, are explored

$$\bar{\eta}(z)=\exp(\ln(\zeta)(1-z)) \tag{33a}$$
$$\bar{\eta}(z)=\exp(\ln(\zeta)(1-z)^{1/3}). \tag{33b}$$

Figures 1 and 2 show the variations of the critical Rayleigh number, Ra_{cr}, with the aspect ratio for the above two viscosity functions for viscosity contrast equal to 5, 25, and 100. Here the critical Rayleigh numbers are obtained by an initial value approach. Time-accurate calculations were performed in each case with a small but random initial temperature perturbation. The flow field was integrated in time until the disturbance growth rate remained a constant. Close to Ra_{cr}, all but the growing eigenmode (if any) will decay rapidly and, after an initial transient period, the growth of the perturbation corresponds to that of the eigenmode. The critical Rayleigh number, Ra_{cr}, corresponding to zero disturbance growth rate was found by interpolation.

It is of interest to consider the effect of depth-dependent properties on vertical resolution requirements. Tables I and II summarize non-dimensional linear disturbance growth rates for viscosity variations given by Eqs. (33a) and (33b), respectively.

In Table I, the first row of data corresponds to the constant properties case, while the second row of data, with

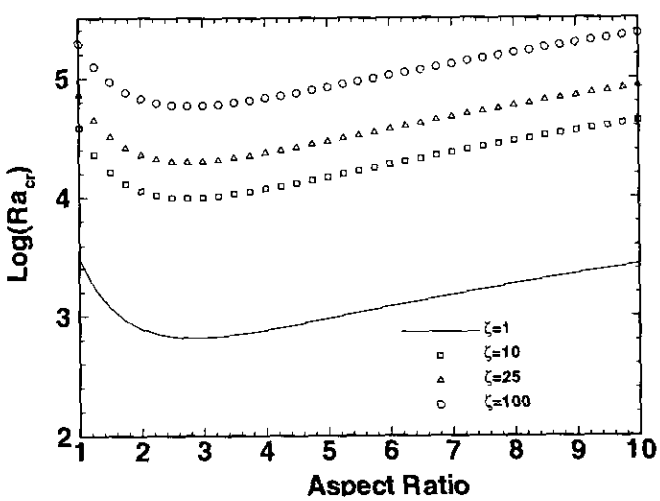

FIG. 1. Critical Rayleigh number vs aspect ratio for depth-dependent viscosity variation given by Eq. (33a) for four different bottom to top viscosity contrasts.

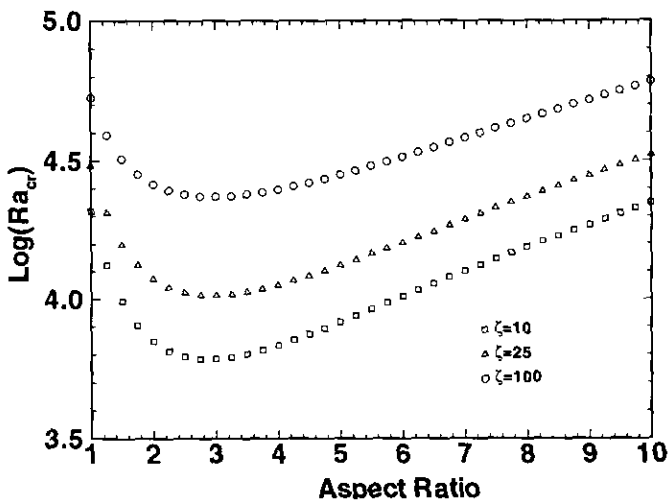

FIG. 2. Critical Rayleigh number vs aspect ratio for depth-dependent viscosity variation given by Eq. (33b) for four different bottom to top viscosity contrasts.

TABLE I

Convergence Test of Linear Growth Rates for Depth-Dependent Properties (Eqs. (32), (33a))

ζ	Ra	$N_z = 15$	$N_z = 35$	$N_z = 55$
1	660	0.05627	0.05627	0.05627
	665	0.16922	0.16922	0.16922
	670	0.28203	0.28203	0.28203
				(Constant properties case)
1	1864	0.04565	0.04565	0.04565
	1874	0.15923	0.15923	0.15923
	1884	0.27259	0.27260	0.27260
10	6090	0.03002	0.03002	0.03002
	6120	0.13526	0.13526	0.13526
	6150	0.24033	0.24033	0.24033
25	10350	0.06962	0.07021	0.07021
	10400	0.17376	0.17435	0.17435
	10450	0.27773	0.27831	0.27831
100	23550	0.03714	0.03740	0.03744
	23650	0.13023	0.12788	0.12788
	23750	0.22326	0.22088	0.22088

$\zeta = 1$, corresponds to the case when viscosity is depth independent but all other properties vary with depth according to Eq. (32). In both these cases 15 grid points in the vertical direction provide adequate resolution, indicating that rapid convergence to the correct result is not affected by vertical variations in adiabatic density, temperature, thermal expansivity, and thermal conductivity. Exponential viscosity variations given by Eq. (33) provide a more stringent test for convergence. In the case of simple exponential increase in viscosity with depth (Table I), the number of vertical grid points required for convergence modestly increases with viscosity contrast parameter ζ. The exponential convergence is destroyed with the use of Eq. (33b) for viscosity variation. A log–log plot of error against the number of grid points reveals algebraic convergence for this viscosity variation. From Table II it can be verified that the order of accuracy depends on the viscosity contrast and ranges from 2.0 to 2.25. The loss of exponential convergence can be attributed to the singularities present in the derivatives of the viscosity function given by Eq. (33b). Although the polynomial expansion inherent in the Chebyshev representation smooths this singularity in the numerical representation, its effect can be clearly seen in the slow convergence.

TABLE II

Convergence Test of Linear Growth Rates for Depth-Dependent Properties (Eqs. (32), (33b))

ζ	Ra	$N_z = 15$	$N_z = 35$	$N_z = 55$	$N_z = 75$	$N_z = 95$
10	9960	0.005	0.068	0.075	0.077	0.078
	9990	0.069	0.132	0.139	0.141	0.142
	10020	0.133	0.196	0.203	0.205	0.206
25	20000	−0.052	0.029	0.038	0.040	0.041
	20080	0.033	0.114	0.123	0.126	0.127
	20160	0.118	0.199	0.208	0.211	0.212
100	59100	−0.066	0.035	0.045	0.049	0.050
	59400	0.043	0.143	0.154	0.158	0.159
	59700	0.151	0.252	0.263	0.266	0.268

Simulations were also conducted in the high Rayleigh number strongly time-dependent regime. Here results obtained at two different Rayleigh numbers, $\mathrm{Ra} = 1.0 \times 10^6$, 1.0×10^7, will be presented. These simulations were performed using the depth-dependent viscosity variation given in Eq. (33a) with a top to bottom viscosity contrast of $\zeta = 10$. A large aspect ratio box of size $5 \times 5 \times 1$ is chosen and the corresponding critical Rayleigh number with the other property variations given by Eq. (32) is 8278.

Steady-state results were obtained for Rayleigh numbers up to 1.5×10^6. In the steady-state regime large scale structures are found with descending sheets and ascending plumes appearing in cylindrical forms, as shown by the isosurface of the temperature field at $T = 0.2$ (Fig. 3a) and $T = 0.5$ (Fig. 3b) for $\mathrm{Ra} = 1.0 \times 10^6$. The planforms are rectangular and owing to the depth-dependent properties, are very different from the corresponding steady-state Boussinesq structures [25]. The temperature isosurface of the plume head spreads horizontally to quite an extent, because of the increase in the vertical velocity of the plume in response to the increasing local Rayleigh number that is due to the decrease in viscosity and the increase in thermal expansivity with height.

At a higher Rayleigh number of 1.0×10^7 (Figs. 4) the flow is strongly time-dependent. A grid resolution of 160×160 Fourier modes and 60 Chebyshev polynomials were used in this simulation. More upmoving plumes appear at random near the bottom boundary and they have a tendency to converge towards a common point at the center of the square planform formed by the downwelling sheets. Such descending sheets have been observed also in the simulation of a compressible mantle in a spherical shell with internal heating [31]. Although the descending boundary layers are primarily sheet-like, many small-scale curvilinear patterns appear and propagate along these downwelling sheets. Visualizations exhibit a flow with two basic time scales: one associated with the large-scale circulation and the other associated with the small-scale boundary layer instability at the top. The time scale of the plume pulsation near the bottom boundary is driven by the large-scale circulatory motion. More detailed results on the nature of this time-dependent high Rayleigh number mantle convection are presented in a recent paper [32].

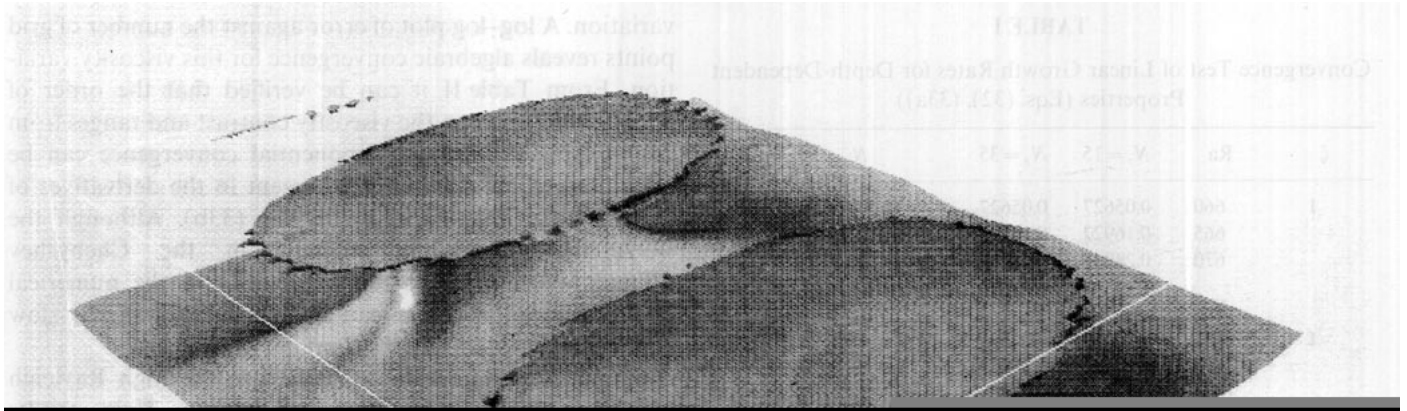

FIG. 3. Isosurface plots of temperature fields for $Ra = 10^6$. Isosurface values of $T = 0.5$ (a) and 0.2 (b) represent respectively ascending circular plumes and descending sheets.

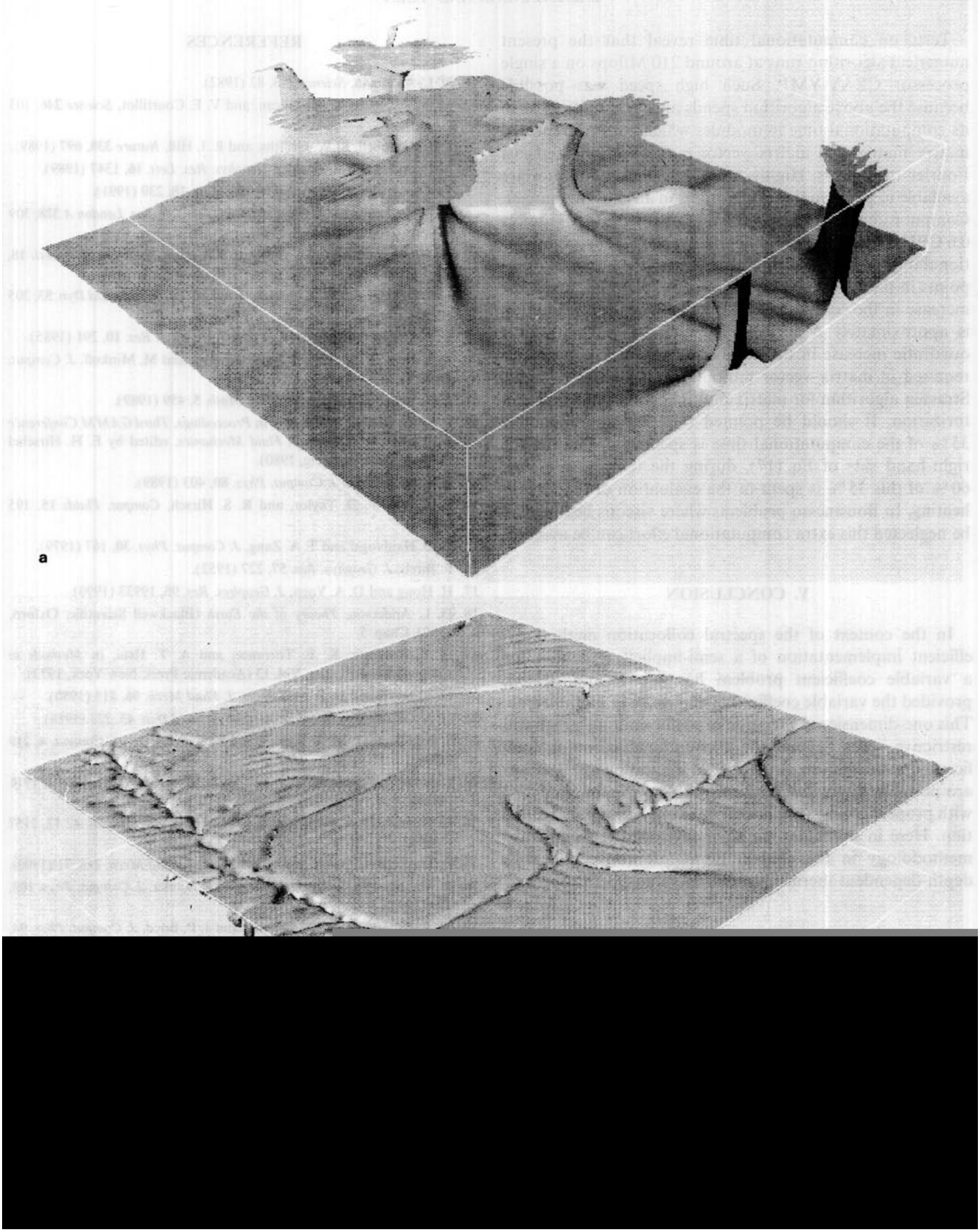

FIG. 4. Isosurface plots of temperature fields for $\mathrm{Ra} = 10^7$. Isosurface values of $T = 0.5$ (a) and 0.2 (b) represent respectively many ascending plumes converging to a common point and descending cold sheets with many small-scale instabilities.

Tests on computational time reveal that the present numerical algorithm runs at around 210 Mflops on a single processor CRAY-YMP. Such high speed was possible because the above algorithm spends approximately 97% of its computational time in modules which perform repeated matrix–matrix and matrix–vector multiplications and fast Fourier transforms. Highly optimized library routines are available to perform these operations in an efficient manner. Computations on a $32 \times 32 \times 55$ grid typically requires 0.6 CPU seconds per Runge–Kutta stage. The computational time almost linearly increases with the number of grid points in the horizontal directions.[2] On the other hand, the increase in the computational time with vertical resolution is approximately $N_z^{1.25}$. This is much less severe than a quadratic increase in the number of arithmetic operations required in matrix–vector multiplication, due to both the Strassen algorithm for matrix multiplication [33] and vectorization. It should be pointed out that approximately 35% of the computational time is spent in evaluating the right-hand side of Eq. (17), during the temperature step; 60% of this 35% is spent in the evaluation of the viscous heating. In Bousinessq problems where viscous heating can be neglected this extra computational effort can be avoided.

V. CONCLUSION

In the context of the spectral collocation method, an efficient implementation of a semi-implicit algorithm for a variable coefficient problem has been demonstrated, provided the variable coefficients depend only on the depth. This one-dimensional variation of coefficients, although still restrictive, goes beyond the conventional constant coefficient approximation. A number of interesting applications are possible where the physical problem can be modelled with properties that vary primarily in only one spatial direction. Here in particular we have developed the numerical methodology in the context of mantle convection with depth-dependent thermodynamic and transport properties.

ACKNOWLEDGMENTS

This research has been supported by the National Aeronautics and Space Administration, the National Science Foundation, and in part by the Army Research Office Contract DAAL03-89-C-0038 with the University of Minnesota Army High Performance Computing Research Center. We thank Connie Lausten and David Reuteler for their help.

[2] Although the CPU time consumed in the FFTs along the horizontal directions increase as $N \log(N)$, the FFTs account for only 20 to 25% of the overall computation.

REFERENCES

1. D. L. Anderson, *Science* **213**, 82 (1982).
2. M. A. Richards, R. A. Duncan, and V. E. Courtillot, *Science* **246**, 103 (1989).
3. I. H. Campbell, R. W. Griffths, and R. I. Hill, *Nature* **339**, 697 (1989).
4. A. Chopelas and R. Boehler, *Geophys. Res. Lett.* **16**, 1347 (1989).
5. M. Osako and E. Ito, *Geophys. Res. Lett.* **18**, 239 (1991).
6. B. H. Hager and M. A. Richards, *Phil. Trans. R. Soc. London A* **328**, 309 (1989).
7. U. Hansen, D. A. Yuen, and S. E. Kroening, *Geophys. Res. Lett.* **18**, 1261 (1991).
8. L. P. Solheim and W. R. Peltier, *Geophys. Astrophys. Fluid Dyn.* **53**, 205 (1990).
9. U. R. Christensen and D. A. Yuen, *J. Geophys. Res.* **10**, 291 (1985).
10. A. Bayliss, D. Gottlieb, B. J. Matkowsky, and M. Minkoff, *J. Comput. Phys.* **81**, 241 (1989).
11. J. M. Augenbaum, *Appl. Numer. Math.* **5**, 459 (1989).
12. L. Kleiser and U. Schumann, in *Proceedings, Third GAMM Conference on Numerical Methods in Fluid Mechanics*, edited by E. H. Hirschel (Vieweg, Braunschweig, 1980).
13. L. S. Tuckerman, *J. Comput. Phys.* **80**, 403 (1989).
14. H. C. Ku, T. D. Taylor, and R. S. Hirsch, *Comput. Fluids* **15**, 195 (1987).
15. D. B. Haidvogel and T. A. Zang, *J. Comput. Phys.* **30**, 167 (1979).
16. F. Birch, *J. Geophys. Res.* **57**, 227 (1952).
17. H. Hong and D. A. Yuen, *J. Geophys. Res.* **95**, 19933 (1990).
18. D. L. Anderson, *Theory of the Earth* (Blackwell Scientific, Oxford, 1989), Chap. 5.
19. D. L. Turcotte, K. E. Torrance, and A. T. Hsui, in *Methods in Computational Physics*, Vol. 13 (Academic Press, New York, 1973).
20. G. T. Jarvis and D. P. McKenzie, *J. Fluid Mech.* **96**, 515 (1980).
21. G. A. Glatzmaier, *Geophys. Astrophys. Fluid Dyn.* **43**, 223 (1988).
22. S. Balachandar, M. R. Maxey, and L. Sirovich, *J. Sci. Comput.* **4**, 219 (1989).
23. L. Sirovich, S. Balachandar, and M. R. Maxey, *Phys. Fluids A* **1**, 1911 (1989).
24. U. Hansen, D. A. Yuen, and S. E. Kroening, *Phys. Fluids A2* **12**, 2157 (1990).
25. B. Travis, P. L. Olson, and G. Schubert, *J. Fluid Mech.* **216**, 71 (1990).
26. R. Madabhushi, S. Balachandar, and P. Vanka, *J. Comput. Phys.* **105**, 199 (1992).
27. M. R. Schumack, W. W. Schultz, and J. P. Boyd, *J. Comput. Phys.* **94**, 30 (1991).
28. C. Canuto, M. Y. Hussaini, A. Quarteroni, and T. A. Zang, *Spectral Methods in Fluid Dynamics* (Springer-Verlag, New York, 1988).
29. T. A. Zang, C. L. Streett, and M. Y. Hussaini, ICASE Report, 89-13, 1989 (unpublished).
30. P. G. Drazin and W. H. Reid, *Hydrodynamic Stability* (Cambridge Univ. Press, Cambridge, UK, 1984).
31. D. B. Bercovici, G. Schubert, and G. Glatzmaier, *Science* **244**, 950 (1989).
32. S. Balachandar, D. A. Yuen, and D. Reuteler, *Geophys. Res. Lett.* **19**, 2247 (1992).
33. V. Pan, *SIAM Rev.* **26**, 393 (1984).